

High resolution modeling of CO₂ over Europe: implications for representation errors of satellite retrievals

D. Pillai¹, C. Gerbig¹, J. Marshall¹, R. Ahmadov^{2,*}, R. Kretschmer¹, T. Koch¹, and U. Karstens¹

¹Max Planck Institute for Biogeochemistry, P.O. Box 100164, 07701 Jena, Germany

²NOAA Earth System Research Laboratory, Boulder, Colorado, USA

* also at: Cooperative Institute for Research in Environmental Sciences, University of Colorado, Boulder, USA

Received: 1 July 2009 – Published in Atmos. Chem. Phys. Discuss.: 30 September 2009

Revised: 10 December 2009 – Accepted: 11 December 2009 – Published: 7 January 2010

Abstract. Satellite retrievals for column CO₂ with better spatial and temporal sampling are expected to improve the current surface flux estimates of CO₂ via inverse techniques. However, the spatial scale mismatch between remotely sensed CO₂ and current generation inverse models can induce representation errors, which can cause systematic biases in flux estimates. This study is focused on estimating these representation errors associated with utilization of satellite measurements in global models with a horizontal resolution of about 1 degree or less. For this we used simulated CO₂ from the high resolution modeling framework WRF-VPRM, which links CO₂ fluxes from a diagnostic biosphere model to a weather forecasting model at 10×10 km² horizontal resolution. Sub-grid variability of column averaged CO₂, i.e. the variability not resolved by global models, reached up to 1.2 ppm with a median value of 0.4 ppm. Statistical analysis of the simulation results indicate that orography plays an important role. Using sub-grid variability of orography and CO₂ fluxes as well as resolved mixing ratio of CO₂, a linear model can be formulated that could explain about 50% of the spatial patterns in the systematic (bias or correlated error) component of representation error in column and near-surface CO₂ during day- and night-times. These findings give hints for a parameterization of representation error which would allow for the representation error to be taken into account in inverse models or data assimilation systems.

1 Introduction

Atmospheric CO₂ has been rising since pre-industrial times due to anthropogenic emissions from fossil fuel combustion and deforestation, which are considered to be major causes of global warming (IPCC, 2007). Climate predictions using coupled carbon cycle climate models differ greatly in their feedbacks between the biosphere and climate, resulting in vastly differing mixing ratios of CO₂ at the end of this century (Friedlingstein et al., 2006). This calls for an improved understanding of biospheric CO₂ fluxes at regional scales. A global network of observations is being used together with modeling tools to derive surface-atmosphere exchanges (via inverse techniques) which can help in quantifying biosphere-climate feedback and assist in monitoring CO₂ trends in the context of climate change mitigation.

However, past studies show that the current observation network is not sufficient to adequately account for uncertainties in surface flux estimates (Gurney et al., 2003). Satellite measurements of column-integrated CO₂ concentrations with better spatial and temporal sampling as well as with adequate precision (~1 ppm) are expected to improve this situation (Rayner and O'Brien, 2001; Miller et al., 2007). Passive satellite missions, such as the Orbiting Carbon Observatory (OCO) (Crisp et al., 2004), and the Greenhouse gases Observatory Satellite (GOSAT) (NIES, 2006) are designed to measure column integrated dry air mole fraction under clear sky conditions using reflected sunlight. GOSAT is now in orbit, but unfortunately the launch of OCO failed. In addition, active sensor missions are under investigation, such as ESA's Earth Explorer candidate mission A-SCOPE, the Advanced Space Carbon and Climate Observation of Planet



Correspondence to: D. Pillai
(kdhanya@bgc-jena.mpg.de)

Earth (ESA, 2008) and NASA's mission ASCENDS, the Active Sensing of CO₂ Emissions over Nights, Days and Seasons, which have the advantage of also being able to measure during the night and thus provide a stronger constraint on respiration fluxes.

The above mentioned satellite measurements are able to provide global coverage of column-averaged CO₂ dry air mole fraction which can improve current estimates of global carbon budgets (via inverse techniques). The footprint sizes of satellite missions using passive sensors (measuring reflected sun light) such as OCO and GOSAT are approximately 1.3 km and 10.5 km, respectively (Crisp et al., 2004; NIES, 2006). Active missions such as A-SCOPE using LIDAR technology, have smaller footprint sizes of around 0.1 km which allows for better sampling under partially cloudy conditions by making use of the cloud gaps (ESA, 2008). However, active missions need some averaging for these 0.1 km footprints to improve the signal-to noise. These footprints are at least an order of magnitude smaller than the highest resolution global inverse models (Peters et al., 2007).

All remote sensing methods to measure atmospheric CO₂ require clear sky conditions, thus a small footprint is desirable since it allows sampling during scattered cloud conditions. On the other hand, the retrievals may not be representative for average CO₂ concentration in such coarse model grids, and may thus introduce a larger representation error (a spatial mismatch of satellite retrievals within larger grid cells). The representation error is expected to depend on the strength and horizontal extent of CO₂ flux variability and on meteorology, both of which influence the variability in atmospheric CO₂. Previous studies show that the representation error increases with decreasing horizontal resolution (Gerbig et al., 2003) and is higher when mesoscale circulation is important (Tolk et al., 2008; Ahmadov et al., 2007). Based on measurements from airborne platforms during the CO₂ Budget and Rectification study (COBRA-2000), Gerbig et al. (2003) concluded that transport models require a horizontal resolution smaller than 30 km to capture important spatial variability of CO₂ in the continental boundary layer, which could be attributed to the spatial variability of surface fluxes. The representation error corresponding to typical global grid cells can be up to 1 to 2 ppm, which is an order of magnitude larger than the sampling errors (Gerbig et al., 2003). The sampling error referred in Gerbig et al. (2003) includes both limitations in instrument precision and accuracy and uncertainty caused by unresolved atmospheric variability of CO₂ within the mixed layer due to turbulent eddies. Further, topography plays a role in representation error. It is reported that representation errors induced by small scale orographic features can be as large as 3 ppm at scales of 100 km (Tolk et al., 2008). van der Molen and Dolman (2007), in their case study around Zotino in Central Siberia, showed that topographic heterogeneity of 500 m within a spatial scale of 200 km can generate horizontal gradients in CO₂ concentrations of 30 ppm. Hence it is highly important to address rep-

resentation errors caused by these spatial mismatches, also for column-integrated measurements from remote sensing, prior to the quantitative assimilation of the information into global modelling systems.

There are a number of studies which have estimated the representation error within a model grid cell when using satellite column measurements. Based on high resolution CO₂ simulations, taking the difference between the simulated grid cell mean and the sampled mean, Corbin et al. (2008) estimated the representation error over North and South America and concluded that satellite retrievals cannot be used in current inverse models to represent large regions with significant CO₂ variability unless transport models are to be run at high resolution. Alkhaled et al. (2008) estimated the representation error based on statistical methods, using spatial covariance information of CO₂ based on model simulation of global CO₂ distribution at a spatial scale of 2° × 2.5° over the sampled regions together with information about the retrieved soundings without the knowledge of the true mean value. Representation errors are quantified using a hypothetical transport model with a spatial resolution of 1° × 1° and a 3 km² retrieval footprint.

This study focuses on estimating possible representation errors of column mixing ratios from remote sensing in global transport models, and on the causes of the spatial variability of CO₂ within a grid cell. Spatial variability of CO₂ is assessed quantitatively based on high resolution simulations for a domain centered over Europe. Using a high resolution transport model, coupled to surface-atmosphere fluxes of CO₂, allows accounting for mesoscale phenomena such as land-sea breeze effects (Ahmadov et al., 2007). Such effects can not be represented in a statistical method as deployed by Alkhaled et al. (2008). We estimate possible representation error as the sub-grid variability of near surface CO₂ and column averages of CO₂ within typical global model grid cells. Hypothetical A-SCOPE track data are used with MODIS cloud pixel information to realistically represent satellite observations. In this context it is relevant to see the possibility of a sub-grid parameterization scheme based on resolved variables to capture the representation error. Such a parameterization scheme could pave the way to describing representation error in coarser models without using high resolution simulations.

The outline of this paper is as follows: Sect. 2 of this paper provides a brief overview of the modeling framework which is used to simulate the CO₂ fields. Section 3 presents the methodology adopted to estimate representation error associated with utilizing satellite column measurements in global inversion studies. In Sect. 4, we present statistical analyses of sub-grid variability of CO₂ fields within grid cells of 100 km × 100 km size to estimate possible representation errors for retrieved satellite column mixing ratios and we investigate correlations of sub-grid variability with resolved variables to assess the possibility of parameterization schemes for representation errors in coarser models.

Table 1. An overview of the WRF physics/dynamics options used.

Vertical coordinates	Terrain-following hydrostatic pressure vertical coordinate
Basic equations	Non-hydrostatic, compressible
Grid type	Arakawa-C grid
Time integration	3rd order Runge-Kutta split-explicit
Spatial integration	3rd and 5th order differencing for vertical and horizontal advection respectively; both for momentum and scalars
Domain configuration	1 domain with horizontal resolution of 10 km; size 2500×2300 km; 31 vertical levels;
Time step	60 s
Physics schemes	Radiation – Rapid Radiative Transfer Model (RRTM) Long wave and Dudhia; Microphysics – WSM 3-class simple ice scheme; Cumulus – Kain-Fritsch (new Eta) scheme (only for the coarse domain!) PBL – YSU; Surface layer – Monin-Obukhov Land-surface – NOAH LSM

2 Modeling framework

We use the modeling system, WRF-VPRM (Ahmadov et al., 2007), which combines the Weather Research and Forecasting model, WRF (<http://www.wrf-model.org/>), with a diagnostic biosphere model, the Vegetation Photosynthesis and Respiration Model, VPRM (Mahadevan et al., 2008). The coupling of these models is done in such a way that VPRM utilizes near surface temperature (T_2) and short wave radiation (SNDOWN) from WRF in order to compute CO₂ fluxes and to provide these to WRF to be transported as a passive tracer.

The principal component of our modelling system consists of a mesoscale transport model, WRF, using the passive tracer transport option from WRF-CHEM (Grell et al., 2005) to simulate the distribution of CO₂ transported by advection, convection and turbulence. Some modifications were made in order to implement simulations of CO₂ transport, which are described in detail in Ahmadov et al. (2007). An overview of the WRF physics/dynamics options used for our simulations is given in Table 1.

The satellite-constrained biosphere model, VPRM is used here to account for CO₂ uptake and emission for different biomes. It is a diagnostic model which uses MODIS (<http://modis.gsfc.nasa.gov/>) satellite indices, the Enhanced Vegetation Index (EVI), and the Land Surface Water Index (LSWI) at 500 m resolution to calculate hourly Net Ecosystem Exchange (NEE). NEE is calculated here as a sum of Gross Ecosystem Exchange (GEE) and Respiration. GEE is calculated by using EVI and LSWI from MODIS, and temperature at 2 m (T_2) and shortwave radiation fluxes (SNDOWN), provided by WRF. Respiration fluxes are calculated as a linear function of WRF-simulated temperature (Mahadevan et al., 2008). To represent land cover in VPRM, we used SYNMAP data (Jung et al., 2006) with a spatial resolution of 1 km and

8 vegetation classes which are suitable for the European domain. The VPRM parameters which control the CO₂-uptake by photosynthesis and the CO₂-emission by respiration for each vegetation class have been optimized using eddy flux measurements for different biomes in Europe collected during the CarboEurope IP experiment (for details see Ahmadov et al., 2007). VPRM captures the spatiotemporal variability of biosphere-atmosphere exchange remarkably well, as shown by comparison with various flux measurements sites corresponding to different vegetation types for longer periods (Ahmadov et al., 2007; Mahadevan et al., 2008). GEE and respiration computed in VPRM is passed on to WRF to simulate the distribution of total CO₂ concentration.

In addition to VPRM biospheric fluxes, anthropogenic and ocean fluxes are included in WRF. High resolution fossil fuel emission data from IER (Institut für Energiewirtschaft und Rationelle Energieanwendung), University of Stuttgart (<http://carboeurope.ier.uni-stuttgart.de/>) are used for the year 2000, at a spatial resolution of 10 km. Temporal emission patterns were preserved by shifting the IER data for 2000 by a few days to match the weekdays in 2003. The total mass of the emissions was conserved when mapping onto the WRF grid. To account for ocean fluxes in WRF, the monthly air-sea fluxes from Takahashi et al. (2002) are used.

Initial and lateral tracer boundary conditions are prescribed from global CO₂ concentration fields based on a simulation by a global atmospheric Tracer transport model, TM3 (Heimann et al., 2003), with a spatial resolution of 4°×5°, and a temporal resolution of 3 h. TM3 is driven by re-analyzed meteorological data from NCEP and surface fluxes optimized by atmospheric inversion (Rödenbeck et al., 2003). As initial and lateral meteorological boundary conditions for WRF, analyzed fields from ECMWF (<http://www.ecmwf.int/>) with a horizontal resolution of approximately 35 km and a 6-h time step are used. The model setup

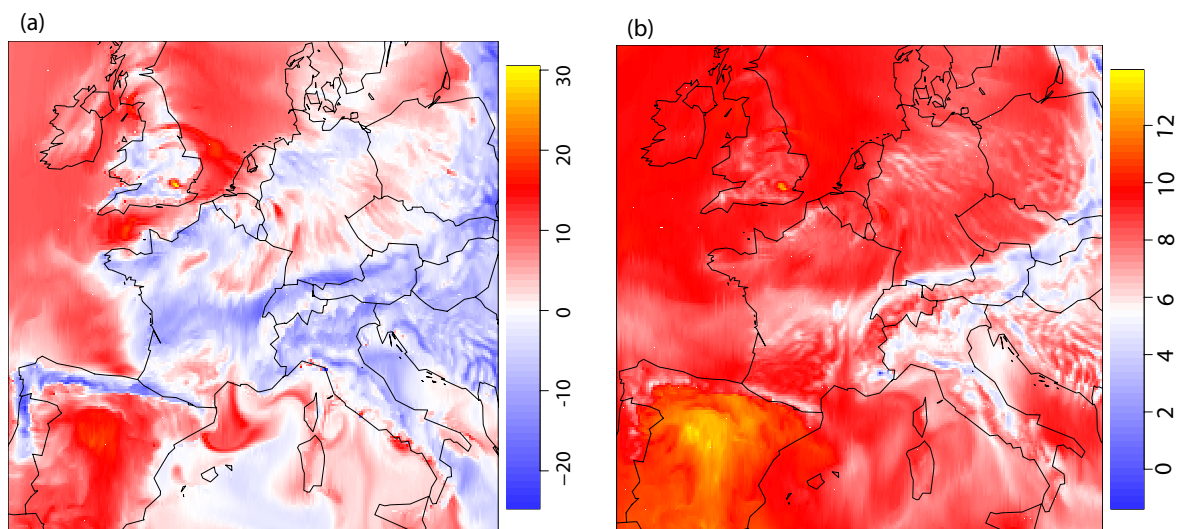


Fig. 1. WRF-VPRM simulations of CO₂ mixing ratios (a) for an altitude of about 150 m above ground (2nd model level), CO_{2,sur} and (b) mass weighted average CO₂ column, CO_{2,col} during 12th July at 14:00 GMT with horizontal resolutions of 10 km for a domain centered over Europe. An offset of 365 ppm is to be added to get total CO₂ in ppm. Note the scale change between near surface and column CO₂.

largely follows the TransCom-continuous protocol (Law et al., 2008), allowing for a comparison of the mesoscale simulation with a number of measurement sites, but also with a large number of global models used for inversion studies. Note however that the anthropogenic and the biospheric fluxes are different from the ones used within the TransCom-continuous Experiment.

Mesoscale simulations are carried out for 2 to 30 July 2003 (29 days of data in total), with a horizontal resolution of 10 km (hereafter referred to as “fine-scale”), and 30 vertical levels extending from the surface up to about 100 mbar for a domain centered over Europe (Fig. 1). Each day of simulation starts at 18:00 UTC of the previous day, and continues for 30 h, of which the first 6 h are used for spin up. These fine-scale simulations attempt to reproduce the atmospheric tracer distribution on scales much closer to the actual footprint of remote sensing instruments (~ 0.1 – 10 km). Model validation has been carried out at a number of measurement sites, and also in comparison with output from TransCom models which are used for global inversion studies. Table 2 shows a summary of statistics of the WRF-VPRM simulation compared to measurements, along with results from two other models used in the TransCom-continuous Experiment, the global model TM3 and the regional model REMO (Chevallard et al., 2002). WRF-VPRM performs reasonably well in comparison to other models for most of the measurement sites, indicated by a high fraction of explained variance (squared correlation coefficient, R^2), but also, more importantly in the context of this study, a quite realistic representation of the variability with relative standard deviations (ratio of modeled to observed standard deviation) close to unity for

most sites. However note that the variability is poorly represented when blending the high resolution fluxes used in WRF (VPRM and IER emissions) with the coarse fluxes used in the TransCom continuous experiment (CASA biospheric fluxes and fossil98 emissions at $1^\circ \times 1^\circ$ resolution); in this case the performance is comparable to REMO also in terms of relative standard deviations (not shown in the table).

3 Methodology

3.1 Calculating representation error for satellite-derived CO₂ columns

Since satellite measurements represent column averages, mass weighted average column CO₂ mixing ratios are calculated from the modeled CO₂ fields. Due to the differences in the averaging kernel for different space-borne sensors, no specific averaging kernel was used. Column averaging excluded the topmost model level in order to exclude boundary effects. The average column CO₂ mixing ratio is thus given by:

$$\text{CO}_{2,\text{col}} = \frac{\sum_{i=1}^{nz} (m_i \cdot \text{CO}_{2,i})}{\sum_{i=1}^{nz} m_i} \quad (1)$$

Here m_i is the dry grid cell air mass and CO_{2,i} is the mixing ratio at model level i , and nz is the number of levels used.

In this context, the term “representation error” refers to possible discrepancies when utilizing satellite information in

current global models, due to the spatial scale mismatches between satellite retrievals and larger model grids. Representation error ($\sigma_{c,col}$) is thus estimated for every time step (hourly) as sub-grid variability (standard deviation of fine-scale CO_{2,col}) within the spatial resolution of current global models. The spatial scale of 100 km is chosen to represent the lower limit of grid cell size found in global models used for inversions. The calculated column averages do not include the entire stratosphere, which amounts to a fraction of 10% of the total atmospheric column (pressure at model top is 100 mbar). Since horizontal variability of CO₂ in the stratosphere on scales below 100 km is small (at least not larger than in the troposphere), neglecting this part of the column might thus result at maximum in a 10% overestimation of the sub-grid variability.

The monthly averaged $\sigma_{c,col}$ (i.e., $c_{,col}$, specific for a given hour of the day) includes random and systematic components of representation errors. It is important to assess which component of this representation error is purely random, i.e. noise introduced by weather, and which part is systematic in nature (the “bias”, or “correlated error” term). Random, uncorrelated errors are expected to decrease when averaging over longer time periods, e.g. for deriving monthly fluxes. In order to exclude random errors, daily values of CO₂ mixing ratios (at a specific time, e.g. 14:00 GMT) are averaged for the whole month and subsequently estimated sub-grid variability from this averaged concentration (i.e., $\sigma_{2,col}$). This gives a representation error ($\sigma_{c,col(bias)}$) that is purely of systematic nature on a monthly time scale. We define the term “bias” introduced here as the part of the error that is correlated over the timescale of a month. Note that the bias component of error is always denoted with subscript “(bias)”.

In addition to $\sigma_{c,col}$, near-surface CO₂ mixing ratios (CO_{2,sur}) at an altitude of about 150 m above the surface (the second model level) are also analyzed in terms of sub-grid variability $\sigma_{c,sur}$. A similar analysis is again carried out for a spatial resolution of 200 km (not shown).

3.2 Using A-SCOPE track information including MODIS cloud information

In order to realistically represent satellite retrievals with our model simulations, we followed the simulated A-SCOPE sampling track. Temporal resolution of the track is 0.5 s, corresponding to a spatial distance between subsequent samples of 3.5 km (F. M. Bréon, Laboratoire des Sciences du Climat et de l’Environnement, personal communication). The samples are initially aggregated to a horizontal resolution 10 km and these 10 km samples are used for further analysis. Note that this aggregation causes the representation error to be underestimated. Since satellite retrievals require clear sky conditions, the simulations are sampled for the pixels with clear sky. Cloud free conditions are picked up based on MODIS cloud pixel information (http://modis-atmos.gsfc.nasa.gov/MOD35_L2/index.html) at 1 km resolution for the period of

Table 2. Statistics for the comparison of WRF-VPRM simulations to measurements, along with results from two transport models used in the TransCom Continuous experiment.

Squared correlation coefficient, R^2			
Station	Model [Horizontal Resolution]		
	WRF-VPRM [10×10 km ²]	REMO [0.5°×0.5°]	TM3_vfg [1.875°×1.875°]
Heidelberg	0.29	0.48	0.37
Hegyhatsal 48m	0.44	0.35	0.28
Hegyhatsal 115	0.41	0.48	0.25
Schauinsland	0.16	0.07	0.06
Mace Head	0.24	0.48	0.29
Monte Cimone	0.38	0.13	0.17
Ratio of modeled to measured standard deviation			
Station	Model [Horizontal Resolution]		
	WRF-VPRM [10×10 km ²]	REMO [0.5°×0.5°]	TM3_vfg [1.875°×1.875°]
Heidelberg	0.95	2.72	1.03
Hegyhatsal 48m	1.21	2.75	1.64
Hegyhatsal 115	1.19	1.61	1.28
Schauinsland	0.99	0.92	0.82
Mace Head	0.6	1.02	0.79
Monte Cimone	1.82	0.65	0.79

simulation. 46 438 samples of cloud free columns are extracted including 27 605 samples (60%) over land. These samples were aggregated to a spatial scale of 100 km along the A-SCOPE track. There is an average of 6.6 cloud free 10 km samples along the A-SCOPE track within each 100 km grid cell. The representation error for A-SCOPE derived CO₂ columns (σ_{ascope}) is calculated as the standard deviations of the difference of 100 km×100 km flight track averages using only A-SCOPE 10 km samples along the flight track, and the 100 km×100 km averages based on all 10 km grid cells (σ [A-SCOPE 100 km averages – true 100 km averages]).

4 Results and discussion

In this section the results based on WRF-VPRM simulations of the distribution of atmospheric CO₂ in July 2003 are presented. An example of the WRF-VPRM output is given in Fig. 1, showing simulated (a) CO_{2,sur} and (b) CO_{2,col} on 12 July at 14:00 GMT. Strong spatial variability of the boundary layer CO₂ can be seen near the coasts (Fig. 1a) due to the 3-D-rectification effect (the temporal covariance between sea-land breeze transport and biosphere-atmosphere fluxes, both of which are radiation controlled) (Ahmadov et al., 2007), which causes respired CO₂ to be advected over the ocean by synoptic winds or by the land-breeze circulation and to be concentrated in a shallow layer due to the lack of vertical mixing over the ocean. There is also strong variability associated with frontal activity towards the north-eastern edge of

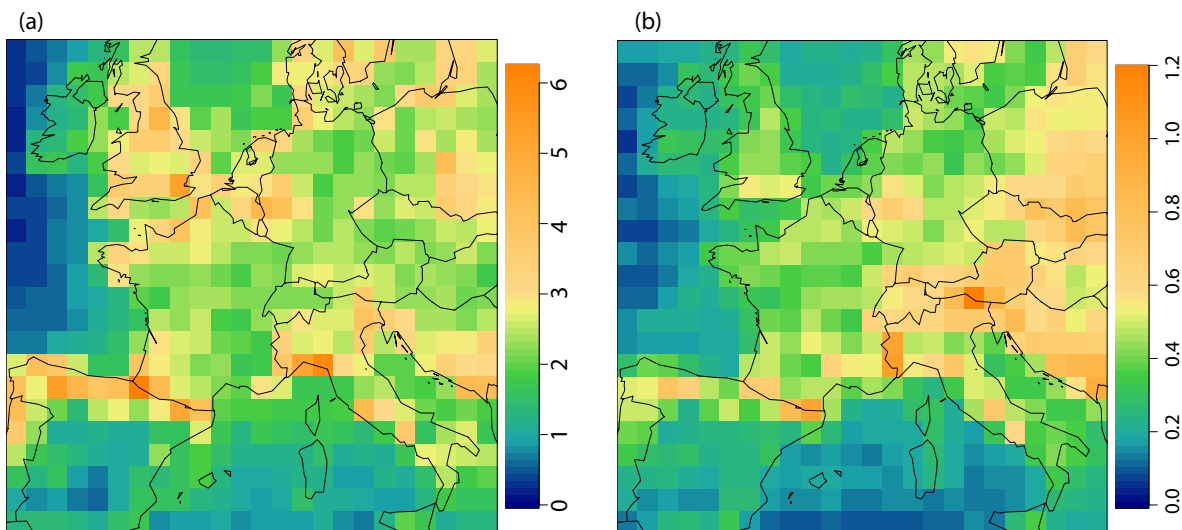


Fig. 2. The monthly averaged subgrid variability of CO₂ concentrations for: (a) near-surface, $\sigma_{c,sur}$ and (b) column average, $\sigma_{c,col}$, for July 2003, using 14:00 GMT only. All values are in ppm.

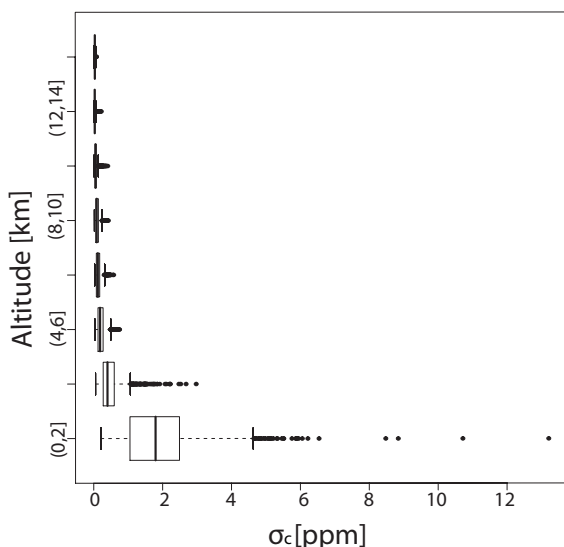


Fig. 3. Box and whisker plot for different altitudes (from ground) ranges of the sub-grid concentration variability (σ_c) for July 2003 (14:00 GMT only). Boxes indicate the central 50%, the bar across the box is the median value, and whiskers indicate the range of the central 95% of data points. Individual data points are shown outside the central 95%.

the domain, with strong gradients in CO₂ associated with the location of a cold front. Such behavior has previously been reported (Parazoo et al., 2008), and has been attributed to the deformational flow along the fronts. A similar pattern is followed in the CO₂ column average (Fig. 1b) near coasts as well as towards the north-eastern edge of the domain, which suggests a strong contribution of boundary layer concentra-

tions to column averages. Movies showing the complete simulation can be seen at:

http://www.bgc.mpg.de/bgc-systems/news/near-surface_co2.html and http://www.bgc.mpg.de/bgc-systems/news/column_co2.html

4.1 Subgrid variability of near surface and column averages of CO₂ concentrations

Figure 2 shows the monthly averaged $\sigma_{c,sur}$ and $\sigma_{c,col}$ (at 14:00 GMT only) for July 2003. Coastal and mountain regions are distinct, with strong sub-grid variability both in near surface and in column averages of CO₂ concentrations. This is due to relatively strong gradients of surface fluxes in these regions.

The similarity in spatial patterns of $\sigma_{c,col}$ and $\sigma_{c,sur}$ (Fig. 2a and b) indicates that the CO₂ column values are correlated with surface values. Figure 3 shows the profile distribution of monthly averaged (at 14:00 GMT) σ_c within different bins of vertical model levels. Most of the higher values of σ_c are found to be within the lowest 2 km. σ_c strongly decreases with increasing altitude, showing less influence of surface fluxes at higher altitudes. These results are consistent with van der Molen and Dolman (2007) which shows that the effect of surface heterogeneity is generally observed in lower atmospheric layers. This indicates the dominance of boundary layer concentration variability in column averages. These dominances can be significant during synoptic scale events, where CO₂ column variability is strongly correlated (squared correlation coefficient, $R^2=0.37$) to boundary layer concentrations (see Fig. 1), but not strongly correlated (squared correlation coefficient, $R^2=0.12$) to concentrations in the free troposphere around 4 km (not shown).

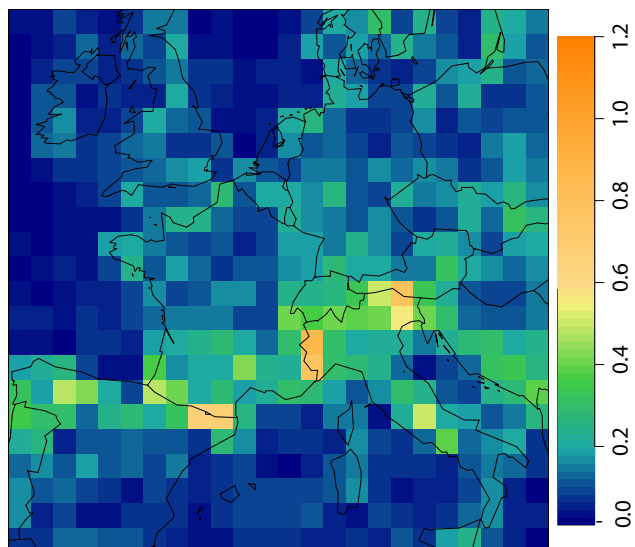


Fig. 4. The monthly averaged subgrid variability of temporally aggregated CO₂ column averages (bias) [ppm] for July 2003, using 14:00 GMT only.

The analysis shows that the monthly averaged $\sigma_{c,col}$ for the domain is, on average, 0.4 ppm, with maximum values around 1.2 ppm and the 90% percentile 0.6 ppm (see Fig. 2). Partitioning the data into ocean and land pixels shows that $\sigma_{c,col}$ is more than twice as large over land (0.5 ppm) as compared to over ocean areas (0.2 ppm) as is expected due to the stronger magnitude and variability of terrestrial fluxes. This is not negligible compared to the targeted accuracy of future satellite retrievals. The monthly bias error, $\sigma_{c,col(bias)}$, is smaller than the full error, but shows a similar pattern with maximum values around 0.9 ppm for mountain and coastal regions (Fig. 4).

4.2 Representation error for satellite derived CO₂ columns

4.2.1 Hypothetical satellite track

Representation errors are quantified here using a hypothetical satellite track going through each 100 km × 100 km cell. Following the sampling conditions used by Alkhaled et al. (2008) (hereafter referred to as A08), we assumed two spatial distributions of satellite retrievals: (1) a full North-South swath (10 pixels from south to north) in each grid cell (idealized sampling condition), and (2) a single retrieval at the corner of each grid cell (adverse sampling condition). The representation errors of hypothetical satellite-derived CO₂ columns (σ_{hypo}) are estimated for these two spatial distributions of satellite retrievals within each 100 km × 100 km grid cell. Figure 5 shows the distribution of σ_{hypo} for a full North-South swath at the center of each 100 × 100 km grid cell. The σ_{hypo} for the previously mentioned sampling con-

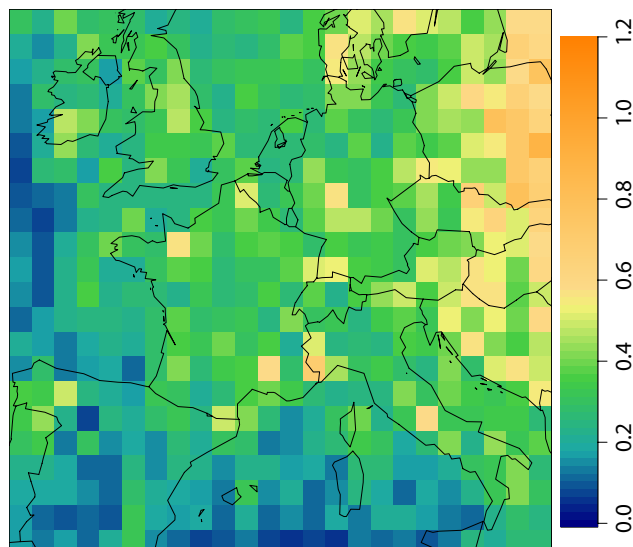


Fig. 5. The subgrid variability of column averages of CO₂ concentrations [ppm] based on hypothetical north-south swath at the center of each 100 km grid cell for July 2003 (monthly averaged at 14:00 GMT).

ditions are estimated and compared with A08 in July for the European domain, and are given in Table 3. The larger representation errors are seen over land for both sampling conditions, and are about a factor of two larger when compared to ocean (see Table 3). The statistical approach suggested by A08 gives much smoother behaviour compared to our results and also neglects land-ocean differences in the European domain. Under idealized sampling conditions (10 pixel swath), the representation error estimates are nearly an order of magnitude larger than those by A08, and under adverse sampling conditions (single corner pixel) our estimates are a factor of two larger compared to those provided by A08 (Table 3).

This finding is in line with experimental evidence: A08 found agreement between their estimates and observation-based estimates from Lin et al. (2004), however the latter were a conservative (low-end or lower limit) estimate of subgrid variability. In fact the power variogram model used by Lin et al. (2004) underestimated the observed variogram estimates by a factor of 3 to 5 at scales smaller than 200 km (see Fig. 2 in Lin et al. (2004)). This corresponds to about a factor two differences in single pixel representation error, which is remarkably similar to the factor found between the high-resolution model based estimate and the one provided by A08. This suggests that it is not generally possible to extract information about the representation error from coarse model simulations as suggested in A08. Such a method is likely to fail in cases of mesoscale complexity.

Table 3. The possible representation error when using A-SCOPE and hypothetical satellite tracks for different sampling conditions. The values given in square brackets indicate monthly bias component. All values are in ppm.

Representation error	All	Land	Ocean	Alkhaled et al. (2008), EU domain*
Hypothetical Satellite (Single corner pixel)	0.59 [0.22]	0.72 [0.28]	0.35 [0.09]	0.30–0.40
Hypothetical Satellite (North-South Swath)	0.38 [0.16]	0.46 [0.20]	0.24 [0.05]	0.04–0.06
ASCOPE	0.34 [0.12]	0.39 [0.15]	0.30 [0.08]	

* extracted from Alkhaled et al. (2008), Fig. 2c and d for our domain.

4.2.2 A-SCOPE 100 km averages

σ_{ascop} is evaluated using the A-SCOPE satellite track information as described in Sect. 3.2. When combining all A-SCOPE samples within each 100 km grid cell, the resulting representation error σ_{ascop} is reduced compared to the single pixel error. Note that this is due to the fact that several pixels contribute to each A-SCOPE sample, whose error can partially cancel out. As for the hypothetical satellite tracks, larger representation errors for A-SCOPE are seen over land (0.4 ppm) as compared to over ocean areas (0.3 ppm) (Table 3).

4.3 Dependence of representation error on explanatory variables

Knowledge about the size and the spatial and temporal patterns of the representation error is expected to improve inverse modeling of satellite data, but this would involve using a high resolution model to estimate the representation error. Our goal is to construct a linear model based on a subset of those explanatory variables which explains a significant fraction of sub-grid variability, and which can be used in the context of global inverse modelling to capture the spatiotemporal patterns. Such a linear model is the simplest subgrid parameterization scheme for representation errors in coarser models, only accounting for local effects and neglecting any effects from advection of subgrid variability.

Statistical relationships between the representation error and the following variables are explored (not shown): the standard deviation of the fluxes (σ_f), the mean of the fluxes (\bar{f}), the absolute mean of the fluxes ($|\bar{f}|$), the mean terrain height (\bar{h}), standard deviation of the terrain heights (σ_h) and the mean mixing ratio near the surface (\bar{c}). \bar{c} is included since it can be expected that variability is associated with the magnitude of the mixing ratios. The analysis showed that the representation error is best explained by the variables σ_h , σ_f

Table 4. The statistical estimation (squared correlation coefficient) of the bias component of the representation error ($\sigma_{c(\text{bias})}$) explained by each variable and the proposed linear model.

Explanatory Variables	Day-time		Night-time	
	Column $\sigma_{c,\text{col}}$	Surface $\sigma_{c,\text{sur}}$	Column $\sigma_{c,\text{col}}$	Surface $\sigma_{c,\text{sur}}$
σ_f [$\mu\text{moles}/\text{m}^2 \text{s}^{-1}$]	0.34	0.66	0.09	0.13
σ_h [m]	0.51	0.20	0.59	0.33
\bar{c} [ppm]	0.18	0.09	0.02	0.16
Linear model with σ_f, σ_h & \bar{c}	0.63	0.67	0.63	0.46

and \bar{c} during day-time as well as night-time. Hence a linear model is constructed using three variables: σ_h , σ_f and \bar{c} . Table 4 gives the statistical estimation of the variability explained by each of these variables. In addition to $\sigma_{c,\text{col}}$, we also investigated the same linear model for $\sigma_{c,\text{sur}}$. The explained variability by each of these variables differs between day- and night-time, also between column and near-surface mixing ratios. The proposed linear model has the same variable structure, but different coefficients for the explanatory variables.

Figure 6 shows the dependence of $\sigma_{c,\text{col}(\text{bias})}$ on each of these variables. Figure 6a shows a monotonic increase of $\sigma_{c,\text{col}(\text{bias})}$ with increasing σ_f at the 100 km scale and explains 34% of $\sigma_{c,\text{col}(\text{bias})}$ during day-time, however the relationship with σ_f is absent during night-time (Fig. 6d). It is found in general that $\sigma_{c(\text{bias})}$ is well explained by σ_f (34% of the total column variability and 66% of the surface variability) during day-time; however correlations are weaker during night-time (Table 4). This can be explained as follows: the fluxes are larger and more spatially variable during daytime than during nighttime. In addition, strong vertical mixing during day-time couples the mixing ratios over a deeper part of the column to the patterns in surface fluxes, while during night there is less vertical mixing, with more advection and drainage flow in the stable nocturnal boundary layer, smearing out the signatures from patchy surface fluxes.

The effect of heterogeneity in topography on $\sigma_{c,\text{col}(\text{bias})}$ can be seen in Fig. 6b and e. $\sigma_{c,\text{col}(\text{bias})}$ increases in response to increase in σ_h and explains good fraction (51–59%) of sub-grid variability of mixing ratios. Nocturnal $\sigma_{c,\text{sur}(\text{bias})}$ is more correlated with σ_h (33%), rather than day-time $\sigma_{c,\text{sur}(\text{bias})}$ (20%) (see Table 4; not shown the figure). This shows that topography has more influence on representation error of CO₂ concentrations in the lower boundary layer during night when transport is more dominant than surface flux variability.

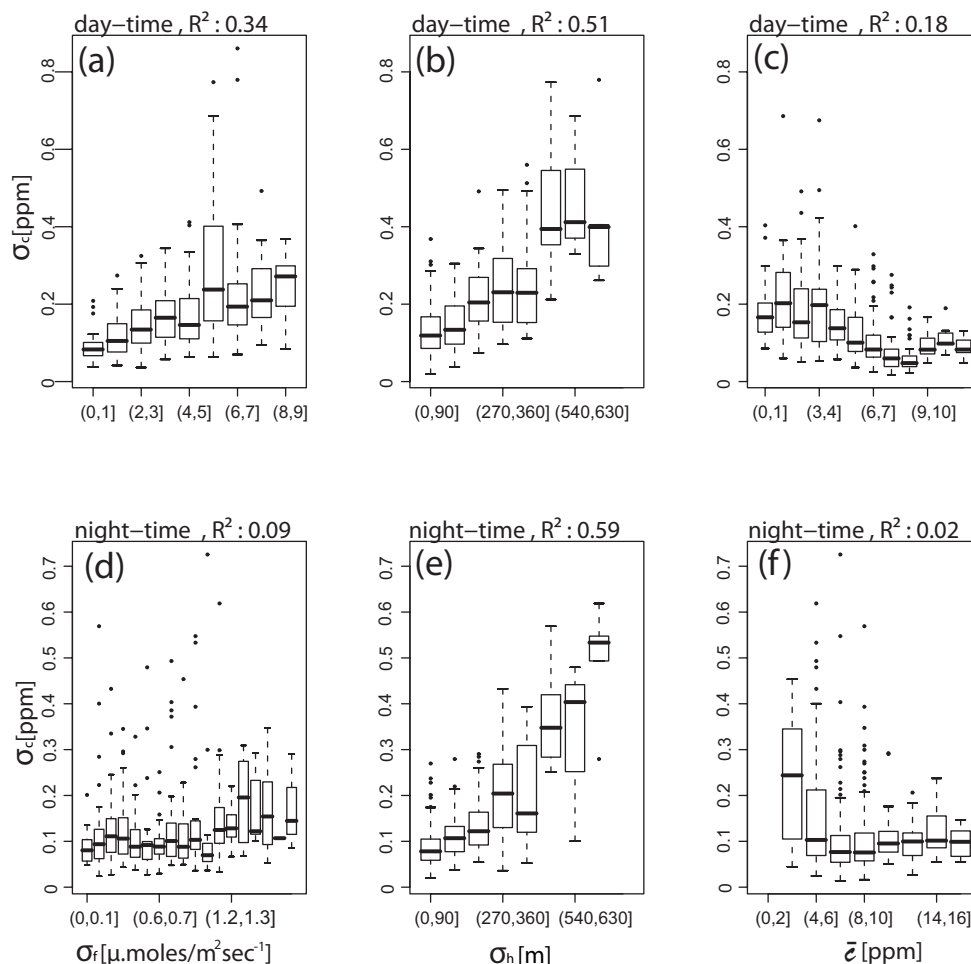


Fig. 6. Distribution of the bias component of column CO₂ sub-grid variability ($\sigma_{c,\text{col}}(\text{bias})$) on **(a, d)** σ_f , **(b, e)** σ_h , **(c, f)** \bar{c} for July 2003 [(a)–(c): 14:00 GMT only, (d)–(f): 02:00 GMT only]. Boxes indicate the central 50%, the bar across the box the median, and whiskers the central 95%. Individual data points are shown outside the central 95%.

\bar{c} is negatively correlated with $\sigma_{c,\text{col}}(\text{bias})$ during day-time (see Table 5) and explains 18% of variability, whereas the correlation is absent during night-time (Fig. 6c and f). In contrast to this, the correlation of \bar{c} with $\sigma_{c,\text{sur}}(\text{bias})$ is absent during day-time, but explains 16% of nocturnal variability (Table 4).

The linear model using all three variables explains about 50% of the spatial patterns in the (monthly) bias component of sub-grid variability during day- and night-times (Table 4). It is found that nocturnal $\sigma_{c,\text{sur}}$ is better explained (60% in comparison to 46%) by the linear model when including the variable \bar{f} , however no further improvements for $\sigma_{c,\text{col}}$ or day-time $\sigma_{c,\text{sur}}$ are found (not shown). Figure 7 illustrates how well the representation error is captured with the proposed linear model. It seems therefore possible to introduce this parameterization of representation error in coarser models so that data assimilation systems using coarser transport models can use realistic estimates for representation errors that have the appropriate spatial and temporal dependence.

Table 5 gives the linear model coefficients for each of these explanatory variables. Note that coefficients are horizontal scale dependent, and we expect them to also vary between seasons due to differences in flux patterns and transport characteristics.

The implementation of the proposed parameterization scheme in global models requires these three explanatory parameters: σ_h can be easily calculated from any high resolution topographic elevation data, for example USGS GTOPO dataset (http://eros.usgs.gov/#/Find_Data/Products_and_Data_Available/GTOPO30). The information on fluxes (σ_f) can be accessed from biosphere models with high spatial resolution, e.g. VPRM. \bar{c} is represented in global model simulations or from the satellite retrievals. However, care has to be taken to remove long term trends and seasonal cycles when simulating longer periods, otherwise representation error estimates would be falsely influenced by these. Such a simple parameterization would likely reduce the impact of representation errors significantly, although an inverse

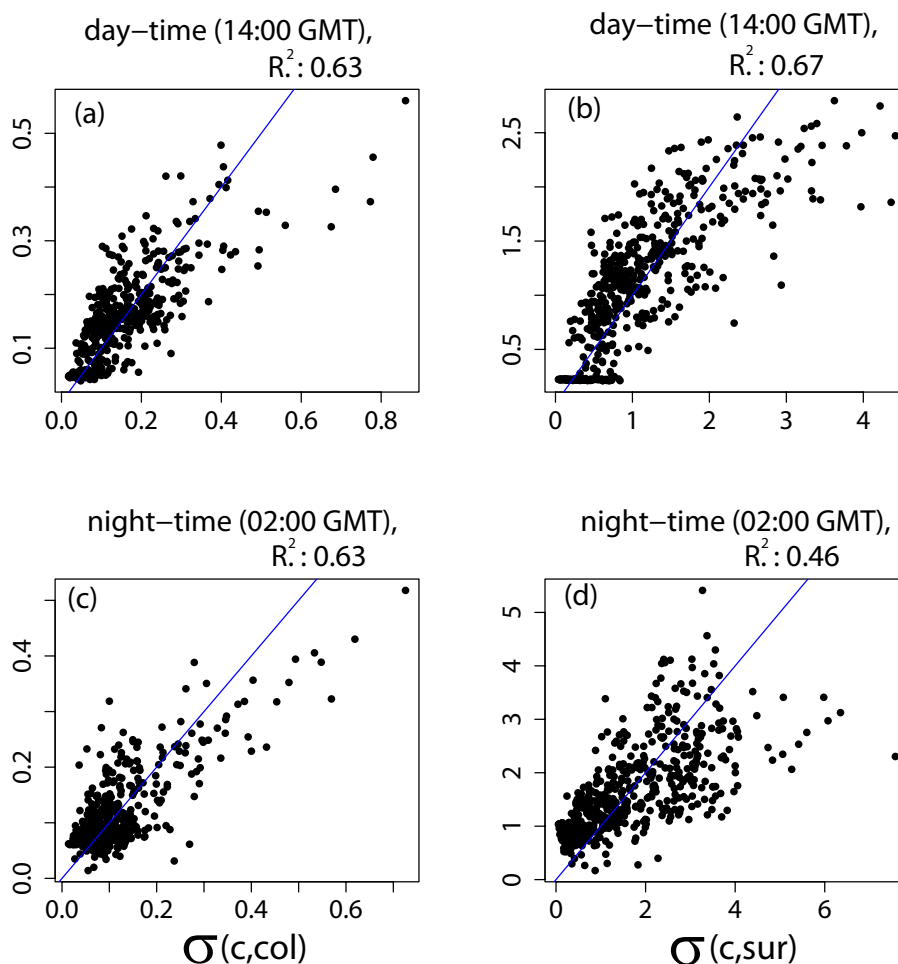


Fig. 7. The linear model (bias) estimates of representation error (X-axis) compared to the values from the WRF-VPRM simulations (Y-axis) for (a,c) column averages, $\sigma_{c,col}(\text{bias})$ and (b,d) near-surface, $\sigma_{c,sur}(\text{bias})$ for July 2003 [(a)–(b): 14:00 GMT only, (c)–(d): 02:00 GMT only]. The 1:1 line is shown in blue.

modeling study would be required to investigate the reduction of the impact on flux retrievals.

5 Summary and outlook

Satellite retrievals of column CO₂ provide a global coverage of measurements; these often correspond to small footprints of the order of a few kilometers or less. Our analysis of high resolution WRF-VPRM fields of CO₂ show that when these column retrievals representing small spatial scales are used in inverse studies with current global transport models with grid sizes of 100 km, the scale mismatches can introduce representation errors of up to 1.2 ppm, which is above the targeted precision of most satellite measurements. This may lead to a systematic bias in flux estimates when using inverse modeling approaches.

Compared to estimates based on variogram analysis of coarse models (Alkhaled et al., 2008), representation errors for a full swath of 10 km width of a hypothetical satellite (idealized sampling condition) were found to be nearly an order of magnitude larger. This clearly shows the necessity of using high resolution simulations to assess variability on scales not resolved by global models. The analysis with ASCOPE track data together with MODIS cloud pixel information shows a larger representation error (0.39 ppm) over land compared to other regions.

Furthermore, we attempted to model sub-grid scale variability (or representation error) as a linear function of local, grid-resolved variables. A linear model is constructed separately for day- and night-times as well as for column and near-surface, which has the same variable structure (σ_h , σ_f and \bar{c}), but different coefficients for the explanatory variables. The proposed linear model (using all three variables) could explain about 50% of the spatial patterns in the bias component of sub-grid variability during day- and night-

Table 5. Coefficients of the linear model for the monthly bias component of the representation error ($\sigma_{c(\text{bias})}$). The standard errors of the coefficients are given in curly brackets.

	Day-time				Night-time			
	Column		Surface		Column		Surface	
	$\sigma_{c,\text{col}}$ $\times 10^{-2}$		$\sigma_{c,\text{sur}}$ $\times 10^{-2}$		$\sigma_{c,\text{col}}$ $\times 10^{-2}$		$\sigma_{c,\text{sur}}$ $\times 10^{-2}$	
Resolution [km×km]	100	200	100	200	100	200	100	200
σ_f [$\mu\text{.moles/m}^2\text{ s}^{-1}$]	1.2 {0.15}	1.7 {0.32}	26.5 {1.03}	34.1 {2.00}	-0.01 {0.60}	0.81 {1.35}	12.6 {10.17}	28.6 {18.91}
σ_h [m]	0.04 {0.00}	0.04 {0.00}	0.07 {0.02}	0.05 {0.03}	0.05 {0.00}	0.05 {0.00}	0.50 {0.03}	0.40 {0.05}
\bar{c} [ppm]	-0.47 {0.07}	-0.40 {0.16}	0.38 {0.47}	0.10 {1.02}	-0.58 {0.09}	-0.91 {0.23}	16.2 {1.50}	17.4 {3.26}
Intercept [ppm]	8.5 {0.58}	11.6 {1.58}	19.3 {4.16}	26.7 {9.85}	10.9 {0.77}	17.1 {2.04}	-27 {13.05}	-18 {28.64}

times. These findings suggest a parameterization which would enable a substantial fraction of the representation error to be taken into account more quantitatively.

Future steps are to implement this parameterization in an inverse modeling system and to assess, using pseudo-data experiments, to what degree biases in retrieved fluxes due to representation errors can be avoided. A further refinement of the method will be to treat the subgrid variance as a tracer itself, allowing for advection of subgrid variance within the coarse transport models similar to the study by Galmarini et al. (2008), with the difference that the focus is not on micro-scale, but rather on mesoscale variability. This would probably allow to better describing the representation error over the ocean near the coasts, which with the current linear (local) model cannot be described. When including such a realistic description of the representation error into a data assimilation system that uses remotely-sensed column CO₂, we expect that the retrieved information, such as regional carbon budgets and uncertainties thereof, will improve significantly.

Acknowledgements. This work has been supported through European Space Agency funding (contract AO/1-5244/06/NL/HE). The authors thank François-Marie Bréon for providing the algorithm to calculate the A-SCOPE track and to select cloud free pixels.

The service charges for this open access publication have been covered by the Max Planck Society.

Edited by: F. Dentener

References

- Ahmadov, R., Gerbig, C., Kretschmer, R., Koerner, S., Neinger, B., Dolman, A. J., and Sarrat, C.: Mesoscale covariance of transport and CO₂ fluxes: Evidence from observations and simulations using the WRF-VPRM coupled atmosphere-biosphere model, *J. Geophys. Res.-Atmos.*, 112, D22107, doi:10.1029/2007JD008552, 2007.
- Alkhaled, A. A., Michalak, A. M., and Kawa, S. R.: Using CO₂ spatial variability to quantify representation errors of satellite CO₂ retrievals, *Geophys. Res. Lett.*, 35, L16813, doi:10.1029/2008GL034528, 2008.
- Chevillard, A., Karstens, U., Ciais, P., Lafont, S., and Heimann, M.: Simulation of atmospheric CO₂ over Europe and western Siberia using the regional scale model REMO, *Tellus B*, 54B, 872–894, 2002.
- Corbin, K. D., Denning, A. S., Lu, L., Wang, J.-W., and Baker, I. T.: Possible representation errors in inversions of satellite CO₂ retrievals, *J. Geophys. Res.-Atmos.*, 113, D02301, doi:10.1029/2007JD008716, 2008.
- Crisp, D., Atlas, R. M., Breon, F.-M., Brown, L. R., Burrows, J. P., Ciais, P., Connor, B. J., Doney, S. C., Fung, I. Y., Jacob, D. J., Miller, C. E., O'Brien, D., Pawson, S., Randerson, J. T., Rayner, P., Salawitch, R. J., Sander, S. P., Sen, B., Stephens, G. L., Tans, P. P., Toon, G. C., Wennberg, P. O., Wofsy, S. C., Yung, Y. L., Kuang, Z., Chudasama, B., Sprague, G., Weiss, B., Pollock, R., Kenyon, D., and Schroll, S.: The Orbiting Carbon Observatory (OCO) mission, *Adv. Space Res.*, 34, 700–709, 2004.
- ESA: European Space Agency Mission Assessment Reports-ASCOPE, online available at: http://esamultimedia.esa.int/docs/SP1313-1_ASCOPE.pdf, 2008.
- Friedlingstein, P., Cox, P., Betts, R., Bopp, L., von Bloh, W., Brovkin, V., Cadule, P., Doney, S., Eby, M., Fung, I., Bala, G.,

- John, J., Jones, C., Joos, F., Kato, T., Kawamiya, M., Knorr, W., Lindsay, K., Matthews, H. D., Raddatz, T., Rayner, P., Reick, C., Roeckner, E., Schnitzler, K.-G., Schnur, R., Strassmann, K., Weaver, A. J., Yoshikawa, C., and Zeng, N.: Climate carbon cycle feedback analysis: Results from the C4MIP model inter-comparison, *J. Climate*, 19, 3337–3353, 2006.
- Galmarini, S., Vinuesa, J.-F., and Martilli, A.: Modeling the impact of sub-grid scale emission variability on upper-air concentration, *Atmos. Chem. Phys.*, 8, 141–158, 2008, <http://www.atmos-chem-phys.net/8/141/2008/>.
- Gerbig, C., Lin, J. C., Wofsy, S. C., Daube, B. C., Andrews, A. E., Stephens, B. B., Bakwin, P. S., and Grainger, C. A.: Toward constraining regional-scale fluxes of CO₂ with atmospheric observations over a continent: 1. Observed spatial variability from airborne platforms, *J. Geophys. Res.-Atmos.*, 108, 4756, doi:4710.1029/2002JD003018, 2003.
- Grell, G. A., Peckham, S. E., Schmitz, R., McKeen, S. A., Frost, G., Skamarock, W. C., and Eder, B.: Fully coupled online chemistry within the WRF model, *Atmos. Environ.*, 39, 6957–6975, 2005.
- Gurney, K. R., Law, R. M., Denning, A. S., Rayner, P. J., Baker, D., Bousquet, P., Bruhwiler, L., Chen, Y.-H., Ciais, P., Fan, S. M., Fung, I. Y., Gloor, M., Heimann, M., Higuchi, K., John, J., Kowalczyk, E., Maki, T., Maksyutov, S., Peylin, P., Prather, M., Pak, B. C., Sarmiento, J., Taguchi, S., Takahashi, T., and Yuen, C.-W.: TransCom 3 CO₂ inversion intercomparison: 1. Annual mean control results and sensitivity to transport and prior flux information, *Tellus B*, 55, 555–579, 2003.
- Heimann, M., Koerner, S., Tegen, I., and Werner, M.: The global atmospheric tracer model TM3, Max-Planck Institut für Biogeochemie, Technical Reports 5, 131 pp., 2003.
- IPCC: Climate Change 2007: Synthesis Report. Contribution of Working Groups I, II and III to the Fourth Assessment Report of the Intergovernmental Panel on Climate Change, edited by: Core Writing Team, Pachauri, R. K., and Reisinger, A., IPCC, Cambridge University Press, Cambridge, 104 pp., 2007.
- Jung, M., Henkel, K., Herold, M., and Churkina, G.: Exploiting synergies of global land cover products for carbon cycle modeling, *Remote Sens. Environ.*, 101, 534–553, 2006.
- Law, R. M., Peters, W., Rödenbeck, C., Aulagnier, C., Baker, I., Bergmann, D. J., Bousquet, P., Brandt, J., Bruhwiler, L., Cameron-Smith, P. J., Christensen, J. H., Delage, F., Denning, A. S., Fan, S., Geels, C., Houweling, S., Imasu, R., Karstens, U., Kawa, S. R., Kleist, J., Krol, M. C., Lin, S.-J., Lokupitiya, R., Maki, T., Maksyutov, S., Niwa, Y., Onishi, R., Parazoo, N., Patra, P. K., Pieterse, G., Rivier, L., Satoh, M., Serrar, S., Taguchi, S., Takigawa, M., Vautard, R., Vermeulen, A. T., and Zhu, Z.: TransCom model simulations of hourly atmospheric CO₂: Experimental overview and diurnal cycle results for 2002, *Global Biogeochem. Cy.*, 22, GB3009, doi:3010.1029/2007GB003050, 2008.
- Lin, J. C., Gerbig, C., Daube, B. C., Wofsy, S. C., Andrews, A. E., Vay, S. A., and Anderson, B. E.: An empirical analysis of the spatial variability of atmospheric CO₂: Implications for inverse analyses and space-borne sensors, *Geophys. Res. Lett.*, 31, L23104, doi:23110.21029/22004GL020957, 2004.
- Mahadevan, P., Wofsy, S. C., Matross, D. M., Xiao, X., Dunn, A. L., Lin, J. C., Gerbig, C., Munger, J. W., Chow, V. Y., and Gottleib, E. W.: A satellite-based biosphere parameterization for net ecosystem CO₂ exchange: Vegetation Photosynthesis and Respiration Model (VPRM), *Global Biogeochem. Cy.*, 22, GB2005, doi:2010.1029/2006GB002735, 2008.
- Miller, C. E., Crisp, D., DeCola, P. L., Olsen, S. C., Randerson, J. T., Michalak, A. M., Alkhaled, A., Rayner, P., Jacob, D. J., Suntharalingam, P., Jones, D. B. A., Denning, A. S., Nicholls, M. E., Doney, S. C., Pawson, S., Boesch, H., Connor, B. J., Fung, I. Y., O'Brien, D., Salawitch, R. J., Sander, S. P., Sen, B., Tans, P., Toon, G. C., Wennberg, P. O., Wofsy, S. C., Yung, Y. L., and Law, R. M.: Precision requirements for space-based XCO₂ data, *J. Geophys. Res.*, 112, D10314, doi:10.1029/2006JD007659, 2007.
- NIES: GOSAT: Greenhouse Gases Observing Satellite, Tsukuba, Japan, 2006.
- Parazoo, N. C., Denning, A. S., Kawa, S. R., Corbin, K. D., Lokupitiya, R. S., and Baker, I. T.: Mechanisms for synoptic variations of atmospheric CO₂ in North America, South America and Europe, *Atmos. Chem. Phys.*, 8, 7239–7254, 2008, <http://www.atmos-chem-phys.net/8/7239/2008/>.
- Peters, W., Jacobson, A. R., Sweeney, C., Andrews, A. E., Conway, T. J., Masarie, K., Miller, J. B., Bruhwiler, L. M. P., P'etron, G., Hirsch, A. I., Worthy, D. E. J., van der Werf, G. R., Randerson, J. T., Wennberg, P. O., Krol, M. C., and Tans, P. P.: An atmospheric perspective on North American carbon dioxide exchange: CarbonTracker, *P. Natl. Acad. Sci. USA*, 104, 18925–18930, 2007.
- Rayner, P. J. and O'Brien, D. M.: The utility of remotely sensed CO₂ concentration data in surface source inversions, *Geophys. Res. Lett.*, 28, 175–178, 2001.
- Rödenbeck, C., Houweling, S., Gloor, M., and Heimann, M.: CO₂ flux history 1982–2001 inferred from atmospheric data using a global inversion of atmospheric transport, *Atmos. Chem. Phys.*, 3, 1919–1964, 2003, <http://www.atmos-chem-phys.net/3/1919/2003/>.
- Takahashi, T., Sutherland, S. C., Sweeney, C., Poisson, A., Metz, N., Tilbrook, B., Bates, N., Wanninkhof, R., Feely, R. A., Sabine, C., Olafsson, J., and Nojiri, Y.: Global sea-air CO₂ flux based on climatological surface ocean pCO₂, and seasonal biological and temperature effects, *Deep-Sea Res. Pt. II*, 49, 1601–1622, 2002.
- Tolk, L. F., Meesters, A. G. C. A., Dolman, A. J., and Peters, W.: Modelling representation errors of atmospheric CO₂ mixing ratios at a regional scale, *Atmos. Chem. Phys.*, 8, 6587–6596, 2008, <http://www.atmos-chem-phys.net/8/6587/2008/>.
- van der Molen, M. K. and Dolman, A. J.: Regional carbon fluxes and the effect of topography on the variability of atmospheric CO₂, *J. Geophys. Res.-Atmos.*, 112, D01104, doi:01110.01029/02006JD007649, 2007.